



HAL
open science

Turbulent transport driven by kinetic ballooning modes in the inner core of JET hybrid H-modes

Neeraj Kumar, Yann Camenen, Sadruddin Benkadda, Clarisse Bourdelle,
Alberto Loarte, Alexei R Polevoi, Fabien Widmer

► To cite this version:

Neeraj Kumar, Yann Camenen, Sadruddin Benkadda, Clarisse Bourdelle, Alberto Loarte, et al.. Turbulent transport driven by kinetic ballooning modes in the inner core of JET hybrid H-modes. Nuclear Fusion, 2021, 10.1088/1741-4326/abd09c . hal-03079035

HAL Id: hal-03079035

<https://hal.science/hal-03079035>

Submitted on 17 Dec 2020

HAL is a multi-disciplinary open access archive for the deposit and dissemination of scientific research documents, whether they are published or not. The documents may come from teaching and research institutions in France or abroad, or from public or private research centers.

L'archive ouverte pluridisciplinaire **HAL**, est destinée au dépôt et à la diffusion de documents scientifiques de niveau recherche, publiés ou non, émanant des établissements d'enseignement et de recherche français ou étrangers, des laboratoires publics ou privés.

Turbulent transport driven by kinetic ballooning modes in the inner core of JET hybrid H-modes

N. Kumar^{1,3}, Y. Camenen¹, S. Benkadda¹, C. Bourdelle²,
A. Loarte³, A.R. Polevoi³, F. Widmer¹ and JET
Contributors*

¹ Aix Marseille University, CNRS, PIIM UMR 7345, Marseille, France

² CEA, IRFM, Saint-Paul-lez-Durance, France

³ ITER Organization, Route de Vinon-sur Verdon, 13067 St. Paul Lez Durance, France

* See the author list of E.H. Joffrin et al, Nucl. Fusion 59, 112021 (2019)

Abstract. Turbulent transport in the inner core of the high- β JET hybrid discharge 75225 is investigated extensively through linear and non-linear gyrokinetic simulations using the gyro-kinetic code GKW in the local approximation limit. Compared to previous studies [J. Citrin et al. 2015 *Plasma Phys. Control. Fusion* **57** 014032, J. Garcia et al. 2015 *Nucl. Fusion* **55** 053007], the analysis has been extended towards the magnetic axis, $\rho < 0.3$, where the turbulence characteristics remain an open question. Understanding turbulent transport in this region is crucial to predict core profile peaking that in turn will impact the fusion reactions and the tungsten neoclassical transport, in present devices as well as in ITER. At $\rho = 0.15$, a linear stability analysis indicates that Kinetic Ballooning Modes (KBMs) dominate, with an extended mode structure in ballooning space due to the low magnetic shear. The sensitivity of KBM stability to main plasma parameters is investigated. In the non-linear regime, the turbulence induced by these KBMs drives a significant ion and electron heat flux. Standard quasi-linear models are compared to the non-linear results. The standard reduced quasi-linear models work well for the $E \times B$ fluxes, but fail to capture magnetic flutter contribution to the electron heat flux induced by the non-linear excitation of low $k_{\theta} \rho_i$ micro-tearing modes that are linearly stable. An extension of the quasi-linear models is proposed allowing better capturing the magnetic flutter flux.

Keywords: plasma, transport, turbulence, quasi-linear, gyrokinetic

1. Introduction

Due to the requirement of high melting temperature, low tritium retention as well as low erosion under high heat and particle fluxes, Tungsten (W) has been considered as a promising candidate for plasma-facing components (PFCs) [1–3] in present as well as in future fusion reactor operating with deuterium-tritium (D-T). However, tokamak operation with metallic plasma-facing components raises issues regarding the control of high-Z impurities in the confined plasma. Accumulation of high Z impurities such as W (atomic number 74, atomic mass 183.84) in the core can lead to a significant reduction of the central plasma temperature due to large radiative power losses resulting from line radiation of partially ionized tungsten atoms. This means that the accumulation of W in the inner core can have highly deleterious effects on fusion performance. Consequently, accumulation of W has to be avoided to keep concentrations in the core plasma less than few $n_W \sim 10^{-5}n_D$ to sustain high Q plasmas [4].

In ITER, the transport of W is expected to be determined by neoclassical and turbulent processes, which strongly depends on the gradients of main ion density and temperature, as well as on rotation profiles. In the central region of JET plasmas, neoclassical transport (diffusion and pinch) tends to determine W peaking, with sometimes a contribution from turbulent diffusion. From mid-radius outwards, W peaking is mostly determined by turbulent transport (diffusion and pinch) [5–7]. To predict the W core transport behaviour accurately in the central part, one needs first to predict the density and temperature gradients of the main ions in this region. Study of turbulent transport in the central part, $\rho < 0.3$, is crucial to this respect because this is the region where W accumulation can take place in ITER [8, 9]. Predicting core transport in the region $\rho < 0.3$ is also very important for the fusion reaction rate. It has, however, not been explored extensively so far, and previous studies mostly focused on the edge and core regions, $\rho > 0.3$.

In the inner core region, the key questions are 1) is the plasma linearly unstable? 2) If yes, is turbulent diffusion sufficient to offset the neoclassical (inward) pinch of W, up to which radius and how sensitive this is to the background gradients? An auxiliary question is whether the quasi-linear (QL) approximation is valid in the inner core and up to which degree standard reduced

quasi-linear models such as QuaLiKiz (QuasiLinear gyroKinetic) [10] or TGLF (Trapped Gyro-Landau-Fluid) [11] can be used in the central zone.

The goal of the present work is to investigate the characteristics of core micro-instabilities and test the quasi-linear approximation using linear and non-linear gyrokinetic simulations in the central zone of the JET hybrid H-mode discharge #75225 using the gyrokinetic code GWK [12] in the local approximation limit. Comparisons with the radial region, $\rho > 0.3$, where extensive analyses were already performed [13–15] are also presented.

The paper is organised as follows: In section 2 the simulation setup and input parameters used for the GWK runs are discussed. Section 3 presents the linear simulation results of the hybrid plasma discharge 75225. The non-linear simulation results are given in section 4. In section 5, quasilinear flux modelling is presented. Finally, we discuss the results and conclude in section 6.

2. Reference plasma and gyrokinetic simulations setup

The JET hybrid H-mode discharge 75225 is chosen for our study. This hybrid discharge of the Carbon wall era was analysed in detail in [13–17]. It has high-quality core profile measurements for electron and main ions (Thomson scattering and charge exchange spectroscopy), no sawteeth ($q > 1$) and no other significant core MHD activity in the selected time interval, $t = 6.0 - 6.5$ s. Numerical simulations are performed using the δf gyro-kinetic code GWK [12] in the local approximation limit. GWK is a gyrokinetic flux tube code used to study micro-instabilities and turbulent transport in magnetic confinement plasmas. It solves the gyro-kinetic (GK) Vlasov equation coupled to Maxwell's equations (Poisson's and Ampere's equations) in the 5-dimensional space. The simulation input parameters are calculated using plasma profiles obtained from Gaussian process regression (GPR) of experimental measurements [18]. The experimental input plasma profiles with GPR fits for the electron density n_e , electron temperature T_e , ion temperature T_i and toroidal rotation frequency Ω_{tor} are shown in figure 1. Simulations are performed for three species (deuterium, electron, and carbon), including parallel magnetic vector potential (δA_{\parallel}) and parallel magnetic field (δB_{\parallel}) fluctuations, rotation

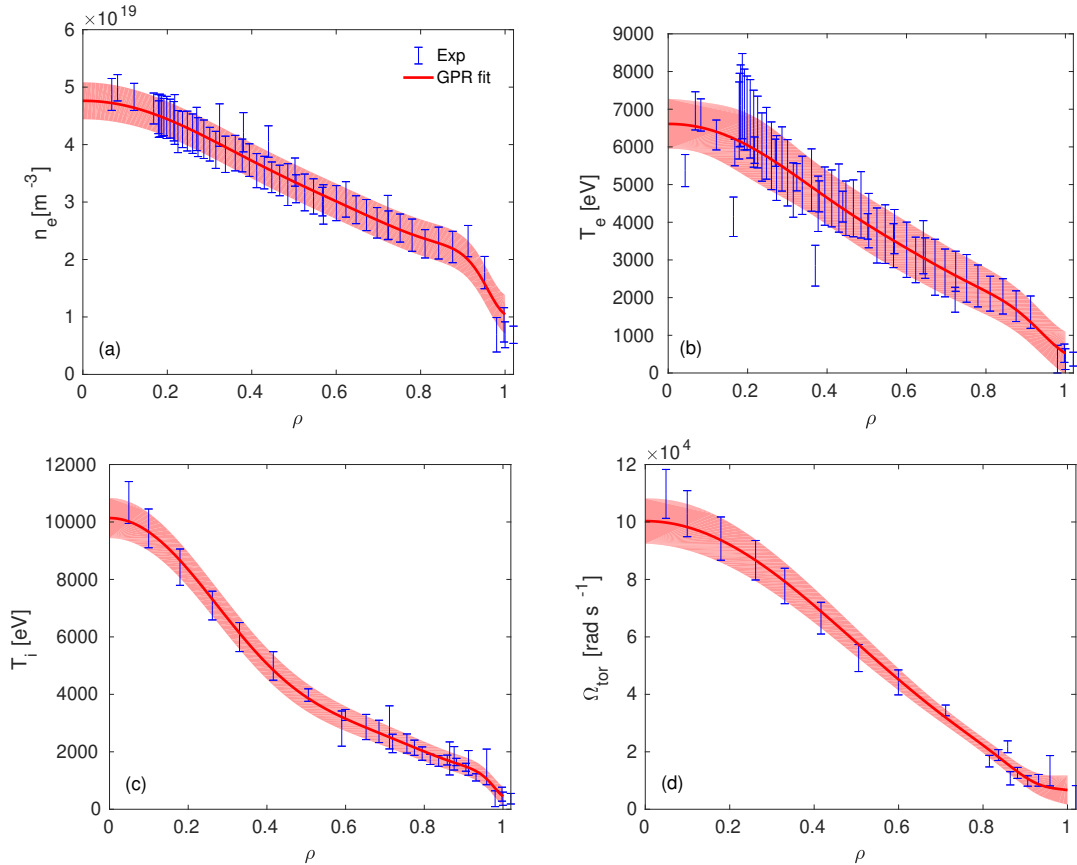


Figure 1: Plasma input profiles obtained from GPR fits of experimental measurements as a function of the normalized toroidal flux ρ for (a) electron density, (b) electron temperature, (c) ion temperature and (d) toroidal rotation frequency. Blue points represent the experimental measured data points with error bars for the JET discharge 75225 and the red (solid) lines show the GPR fit. The shaded area represents the error bars for the GPR fits and all errors are depicted as $\pm 2\sigma$.

(drive from parallel velocity gradient and inertial effects) and collisions. In some cases, the fast ion population from the Neutral Beam Injection (NBI) is added as a fourth species, with a Maxwellian distribution function. Approximating the fast-ion distribution function as a Maxwellian was shown to change the growth rate of ITG modes by about 10% [19]. The magnetic equilibrium is specified using the Miller parametrisation [20]. A linearised Fokker-Planck collision operator is used to model collisions including the pitch-angle scattering, energy scattering and collisional friction terms. All species collisions are retained in the simulations. Following linear grid convergence tests, the typical grid parameters chosen in our linear analysis are as follows: 64 points in the parallel velocity direction, 16 magnetic moments and 32 points discretisation in the parallel direction. The number of poloidal turns is varied from 5 to 50 depending on the value of the magnetic shear and $k_\theta \rho_i$ (more extended mode structure at low magnetic shear and low $k_\theta \rho_i$). The linear stability analysis is carried

out from $\rho = 0.15$ to $\rho = 0.6$, where ρ is the normalised toroidal flux coordinate. The corresponding local plasma input parameters are listed in table 1.

In this table, the normalized gradients for density and temperature are defined as: $R/L_n = -(R_0/n)(\partial n/\partial r)$, $R/L_T = -(R_0/T)(\partial T/\partial r)$, $R_0 = (R_{\min} + R_{\max})/2$ being the reference major radius, T the temperature, n the density and r the minor radius defined as $r = (R_{\max} - R_{\min})/2$, where R_{\max} and R_{\min} are the maximum and minimum major radius of each flux surface respectively. q is the safety factor, $\hat{s} = (r/q)dq/dr$ is the magnetic shear and ν is the reference normalized collisionality from which inter-species collisionalities are computed: $\nu = \frac{n_i e^4 \ln \Lambda^{e/i}}{4\pi \epsilon_0^2 m_e^2 v_{\text{th},e}^3} \frac{R_0}{v_{\text{thref}}}$, with $\ln \Lambda^{e/i}$ the Coulomb

logarithm and $v_{\text{thref}} = \sqrt{2T_{\text{ref}}/m_{\text{ref}}}$ the reference thermal velocity of the considered species. The actual electron to ion collisionality used in the code is enhanced to take into account the impact of impurities not included as a kinetic species (the Z_{eff} value

obtained with the C impurity alone is lower than the actual Z_{eff} value measured from Bremsstrahlung emission). The electron plasma beta is defined as $\beta_e = 2\mu_0 n_e T_e / B_{\text{ref}}^2$. Note that the beta value given in input in GKW is $2\mu_0 n_e T_i / B_{\text{ref}}^2$, which differs for the electron beta by a factor T_i / T_e . Moreover, in the code, the main ion mass is chosen as reference m_{ref} , the equilibrium electron density on the flux surface as n_{ref} , and the ion temperature as T_{ref} . The reference magnetic field B_{ref} is defined as the toroidal magnetic field at R_0 . The normalized toroidal rotation velocity is defined as $u = R_0 \Omega / v_{\text{thref}}$ with $\Omega > 0$ for a plasma flowing in the direction of \mathbf{B} and Ω the angular velocity and u' is the toroidal rotation gradient: $u' = -R_0^2 (\partial \Omega / \partial r) / v_{\text{thref}}$. The radial derivative of the plasma pressure entering the Miller parametrisation is given by $\beta' = (2\mu_0 R_0 / B_{\text{ref}}^2) (dp/dr)$. $\epsilon = r/R_0$ is the inverse aspect ratio, κ the elongation, δ the triangularity, ζ the squareness and their radial derivatives $s_\kappa = (r/\kappa) \partial \kappa / \partial r$, $s_\delta = r \partial \delta / \partial r / \sqrt{1 - \delta^2}$ and $s_\zeta = r \partial \zeta / \partial r$. The radial derivative of the flux surface center major radius and elevation are $R'_{\text{mil}} = \partial R_{\text{mil}} / \partial r$ and $Z'_{\text{mil}} = \partial Z_{\text{mil}} / \partial r$, respectively.

The Miller parametrisation is computed from the EFIT equilibrium reconstruction constrained by MSE measurements and including the fast ion pressure. A separate magnetic equilibrium without the fast ion pressure has been calculated with the CHEASE code [21] and the corresponding Miller parametrisation for this case is listed in table 2. The main difference between the two equilibria is a larger radial derivative of the total pressure, β' , and of the center flux surfaces R'_{mil} for $\rho > 0.3$ when the fast ion pressure is included in the magnetic equilibrium. At $\rho = 0.15$, the nominal value of the magnetic shear is 0.01. At such a low magnetic shear, the distance between resonant flux surfaces $\delta = \frac{1}{nq}$, where $q' = \partial q / \partial r$ and n is the toroidal mode number, becomes comparable to the plasma minor radius and the validity of the ballooning representation may be questioned (although in practice, it depends on the radial mode extent). To be on the safe side, the value of the magnetic shear at this location has therefore been increased to 0.05, which is well within the uncertainty on this quantity. The validity of the ballooning approximation is checked a posteriori in Sec. 3.2 and the impact of the magnetic shear value on the mode growth rate is explored in figure 6.

3. Linear stability

3.1. Overview across the minor radius and impact of fast ions

This section presents the linear simulation results obtained in the core of the JET hybrid H-mode #75225, from $\rho = 0.15$ to $\rho = 0.6$. In figure 2, the linear growth rate and real frequencies spectra are shown at three radial locations $\rho = 0.15$, $\rho = 0.33$ and $\rho = 0.60$, as a function of $k_\theta \rho_i$, where k_θ is the binormal wave vector and $\rho_i = m_i v_{\text{thref}} / (e B_{\text{ref}})$ is the reference ion Larmor radius. In this figure, the impact of the fast ion population is investigated by performing three sets of simulations: 1) with fast ions as a kinetic species and with the fast ion pressure in the magnetic equilibrium (red curve), 2) without fast ions as a kinetic species and without the fast ion pressure in the magnetic equilibrium (green line), 3) without fast ions as a kinetic species and with fast ion pressure in the magnetic equilibrium (blue line). At $\rho = 0.15$, all the linearly unstable modes rotate in the ion diamagnetic drift direction ($\omega_r > 0$) and have a real frequency much larger than their growth rate. These modes are identified as Kinetic Ballooning Modes (KBMs), a point that will be further clarified later in the paper (section 3.2). As often, see e.g. [22], Micro-Tearing Modes (MTM) are obtained at the lowest $k_\theta \rho_i$, characterised by their negative frequency and the even parity of the vector potential fluctuations. In the present case, these MTMs are linearly stable but will matter for the quasi-linear analysis of section 5. Including fast ions as a kinetic species decreases the KBMs growth rate by about 20%, whereas the fast ion pressure in the magnetic equilibrium has almost no impact on the mode growth rate, simply because it has almost no impact on the Miller parameters at this location. At $\rho = 0.6$, the most unstable modes are Ion Temperature Gradient (ITG) modes. Including the fast ions as a kinetic species is found to reduce the mode growth rate, consistently with the previous gyrokinetic analysis performed using the gyrokinetic code GENE [14, 15]. When the fast ion pressure is included in the magnetic equilibrium reconstruction, the ITG mode growth rate increases as observed in [23], where increasing β' in the local Grad-Shafranov equilibrium (i.e. increasing β' keeping the other Miller parameters fixed) first leads to a destabilisation of the ITG. At the intermediate position, $\rho = 0.33$, the situation is more complex. Without fast ions as a kinetic species nor in the magnetic equilibrium, the most unstable mode is an ITG at high $k_\theta \rho_i$ or a KBM at low $k_\theta \rho_i$, as indicated by the jump in the mode frequency. Including the fast ion pressure in the magnetic equilibrium significantly stabilises the KBMs and barely affects the ITG modes. When fast ions

Table 1: Normalized input parameters used in GKW simulations for the JET 75225 discharge selected in the time interval 6.0-6.5 s. The magnetic equilibrium includes the fast ion pressure.

ρ	$\frac{R}{L_{Ti}}$	$\frac{R}{L_{Te}}$	$\frac{R}{L_{Tf}}$	$\frac{T_e}{T_i}$	$\frac{T_f}{T_i}$	$\frac{R}{L_{nC}}$	$\frac{R}{L_{ne}}$	$\frac{R}{L_{nf}}$	$\frac{n_C}{n_e}$	$\frac{n_f}{n_e}$	$\beta_e[\%]$	u	u'	Z_{eff}	ν
0.15	4.23	1.99	1.80	0.69	5.60	-0.70	1.51	0.80	0.01	0.12	3.19	0.32	0.59	1.74	0.015
0.20	5.57	2.70	-0.58	0.72	6.05	-1.13	1.97	-0.88	0.01	0.12	2.96	0.32	0.80	1.74	0.016
0.25	6.60	3.31	2.41	0.76	6.63	-1.45	2.32	1.84	0.01	0.13	2.69	0.32	0.99	1.74	0.017
0.33	7.70	4.09	9.64	0.84	6.05	-1.51	2.74	8.97	0.01	0.10	2.23	0.32	1.31	1.74	0.020
0.40	7.85	4.51	10.71	0.91	7.76	-0.87	2.90	10.24	0.02	0.07	1.85	0.31	1.57	1.74	0.022
0.50	6.30	5.15	4.44	1.04	4.64	2.70	3.15	3.41	0.02	0.06	1.39	0.29	1.88	1.74	0.027
0.60	5.90	5.50	9.61	1.05	4.63	4.41	3.33	7.96	0.02	0.06	1.03	0.24	0.24	1.74	0.035

ρ	ϵ	q	\hat{s}	β'	κ	δ	ζ	s_κ	s_δ	s_ζ	R'_{mil}	Z'_{mil}
0.15	0.05	1.10	0.05	-0.37	1.35	0.02	0.001	-0.004	0.01	0.003	-0.08	-0.005
0.20	0.07	1.10	0.02	-0.48	1.35	0.02	0.001	-0.007	0.02	-0.00	-0.10	-0.008
0.25	0.09	1.11	0.05	-0.57	1.35	0.03	0.001	-0.01	0.03	0.001	-0.12	-0.007
0.33	0.11	1.14	0.21	-0.66	1.34	0.04	0.001	-0.01	0.04	-0.002	-0.16	-0.017
0.40	0.14	1.22	0.49	-0.64	1.34	0.05	0.001	-0.002	0.05	0.001	-0.19	-0.022
0.50	0.17	1.42	0.98	-0.50	1.35	0.06	0.00	0.03	0.09	-0.004	-0.23	-0.026
0.60	0.21	1.74	1.42	-0.37	1.36	0.08	-0.001	0.09	0.14	-0.01	-0.28	-0.063

Table 2: Miller parameters for the magnetic equilibrium without including the fast ion pressure.

ρ	ϵ	q	\hat{s}	β'	κ	δ	ζ	s_κ	s_δ	s_ζ	R'_{mil}	Z'_{mil}
0.15	0.05	1.08	0.05	-0.36	1.31	0.02	0.0024	-0.008	0.02	0.005	-0.08	-0.006
0.20	0.07	1.08	0.02	-0.42	1.30	0.02	0.0003	-0.005	0.02	-0.003	-0.10	-0.006
0.25	0.09	1.09	0.05	-0.45	1.30	0.03	0.0010	-0.008	0.02	0.002	-0.11	-0.007
0.33	0.12	1.12	0.20	-0.42	1.30	0.04	0.0007	-0.00	0.03	-0.002	-0.13	-0.014
0.40	0.14	1.20	0.47	-0.36	1.30	0.04	0.0004	0.015	0.04	-0.002	-0.14	-0.018
0.50	0.18	1.39	0.95	-0.26	1.31	0.06	-0.0003	0.060	0.08	-0.008	-0.17	-0.023
0.60	0.21	1.70	1.40	-0.20	1.33	0.07	-0.0022	0.127	0.13	-0.021	-0.20	-0.053

are included as a kinetic species, the KBM and ITG modes are stabilised, consistently with the picture at $\rho = 0.15$ and $\rho = 0.6$, except at low $k_\theta \rho_i$ where a mode with a higher frequency is excited. This fast ion driven mode was identified as a hybrid BAE (Beta induced Alfvén Eigenmode)/KBM mode in [14,15]. The growth rate of this mode significantly decreases when lowering the kinetic fast ion pressure gradient by 30% (red dashed line in figure 2 (c) and (d)) as noted in [14,15]. Note that the inputs used in the present gyrokinetic simulations slightly differ from those used in [14,15]. For the main species, this is mostly due to the fact that here fits have been done using the recently developed GPR tools [18]. For the fast ion population, the

difference is larger since the present profiles are from the standard PENCIL [24] analysis of JET whereas the ones used in [14,15] were obtained from higher fidelity NEMO-SPOT [25] simulations. The dominant instabilities and the qualitative behaviour with respect to the impact of fast ions are nevertheless similar. The linear stability analysis is then extended to additional radial locations and the maximum linear growth rate is shown as a function of the radial location in figure 3. In the inner core region ($\rho < 0.4$), the dominant mode is found to be a KBM (full symbol). At the mid and outer radius ($\rho \geq 0.4$) it changes to an ITG mode (open symbol). Including fast ions as a kinetic species has a stabilising impact (the difference between blue and red

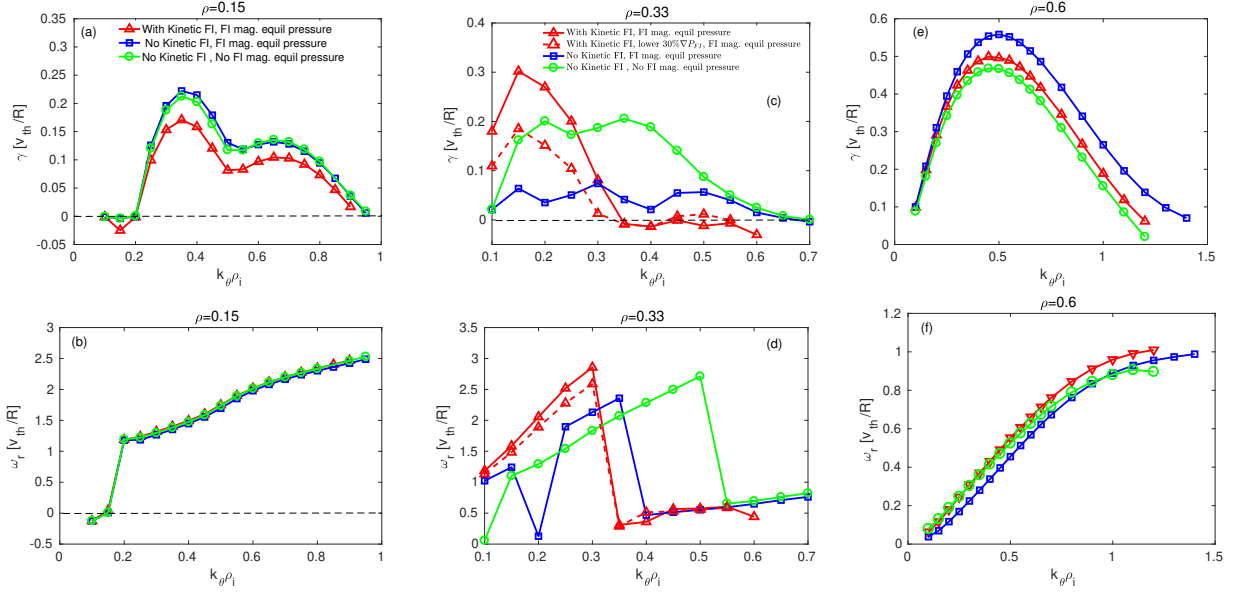


Figure 2: Linear growth rate (top) and real frequency (bottom) spectra as a function of $k_\theta \rho_i$, for the JET discharge 75225 at different radial locations: (a) and (b) at $\rho = 0.15$, (c) and (d) at $\rho = 0.33$, (e) and (f) at $\rho = 0.60$. The green curve represents the case without kinetic fast ions and without fast ion pressure in the magnetic equilibrium. The blue line correspond to the case without kinetic fast ions but the magnetic equilibrium includes the fast ion pressure. The red curve indicates the case with kinetic fast ions and fast ion pressure in the magnetic equilibrium, with the nominal fast ion pressure for the kinetic species (full line) or reduced by 30% (dashed line).

curve) at all radial locations except at $\rho = 0.33$, where it destabilises a BAE/KBM mode (full star symbol) as discussed earlier. Taking into account the fast ions pressure in the magnetic equilibrium stabilises KBMs and slightly destabilises ITGs, consistently with the examples discussed in figure 2. Linear simulations were also performed up to electron scales for $\rho = 0.15$ and $\rho = 0.33$ showing no evidence of Electron Temperature Gradient (ETG) modes destabilisation.

3.2. Linear stability at $\rho = 0.15$

In the following, we will focus on the radial location $\rho = 0.15$, neglecting for the time being the impact of fast ions. The identification of the most unstable mode as a KBM will be supported and its parametric dependencies further documented. Unless otherwise stated, all linear simulations will be performed without fast ions as a kinetic species and with the fast ion pressure included in the equilibrium.

The normalized parallel structure of the perturbed electrostatic potential (ϕ), vector potential (A_\parallel) and magnetic compression (B_\parallel) for the most unstable mode ($k_\theta \rho_i = 0.35$) is given in figure 4 as a function of the parallel coordinate χ at $\rho = 0.15$. The perturbed fields $\delta\phi$, δA_\parallel and δB_\parallel are normalised as follows: $\phi = \alpha_L \frac{e\delta\phi}{\rho_* T_i}$, $A_\parallel = \alpha_L \frac{\delta A_\parallel}{\rho_*^2 B_{\text{ref}} R_0}$, and $B_\parallel =$

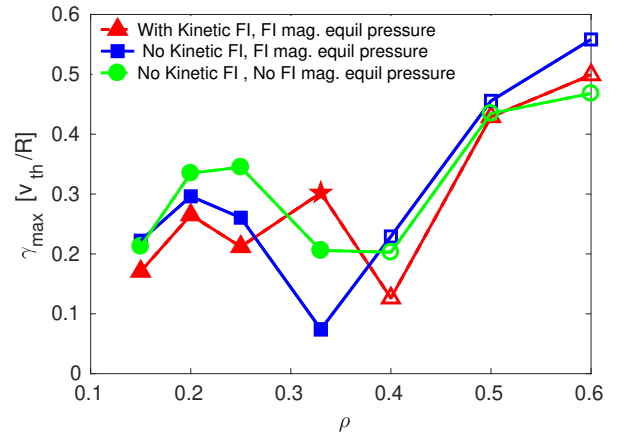


Figure 3: Growth rate of the most unstable modes as a function of radial location ρ , for the JET 75225 discharge. Full symbols are used for KBM modes and open symbols for ITG modes. The (red) full star symbol at $\rho = 0.33$ corresponds to a hybrid BAE/KBM mode destabilised due to kinetic fast ions. Same color code as in figure 2.

$\alpha_L \frac{\delta B_\parallel}{\rho_* B_{\text{ref}}}$ with $\rho_* = \rho_i/R_0$ and α_L an additional normalising factor used in linear simulations to have

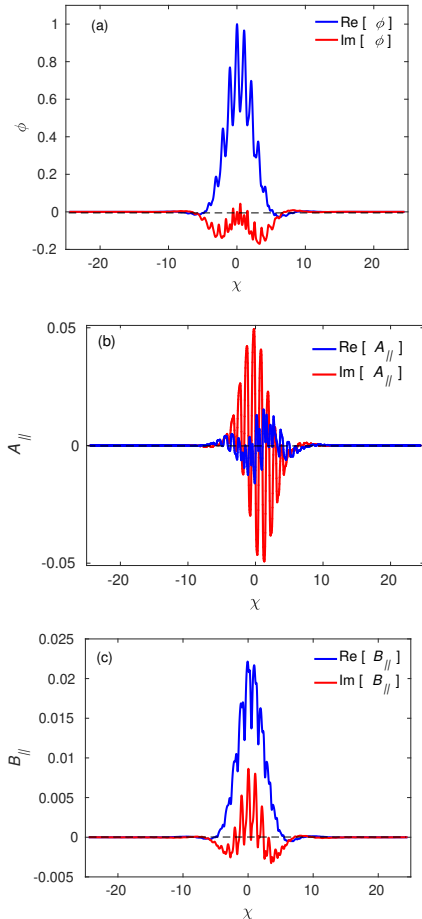


Figure 4: Parallel mode structure of ϕ (a), A_{\parallel} (b) and B_{\parallel} (c), as a function of parallel coordinate χ for the most unstable mode, for the JET 75225 discharge at $\rho = 0.15$ and $k_{\theta}\rho_i = 0.35$. The blue curve represents the real part and the red line indicates the imaginary part.

$\text{Re}[\phi] = 1$ and $\text{Im}[\phi] = 0$ at the χ position where $|\phi|$ is maximum. One poloidal turn corresponds to $\Delta\chi = 1$. The eigenfunctions are characterised by even parity in ϕ and odd parity in A_{\parallel} , with the electrostatic perturbation amplitude higher than the magnetic perturbation amplitude. Note that as a result of the up-down asymmetry of the magnetic equilibrium and the finite values of the background toroidal flow u and parallel flow shear u' which break the parallel symmetry, the parity of the eigenfunction is only approximate. It is important to note that the mode structures are extremely elongated along field lines especially for low wavenumbers and therefore a very high radial resolution was needed (up to 50 poloidal turns at low $k_{\theta}\rho_i$) to properly resolve the modes. The corresponding radial mode width in real space, obtained from a Fourier transform along the

parallel coordinate, is about 5 cm and therefore much smaller than the minor radius $a \sim 1$ m. This validates a posteriori the use of the local approximation at this low magnetic shear values.

As shown in figure 5, varying R/L_{Ti} at fixed R/L_n (blue curve) or varying R/L_n at fixed R/L_{Ti} (red curve) has almost the same impact on the mode growth rate, which suggests that the mode is driven by the ion pressure gradient. The mode growth rate is weakly dependent on the normalised electron temperature gradient R/L_{Te} as seen previously in [26]. The impact of the magnetic shear and the plasma

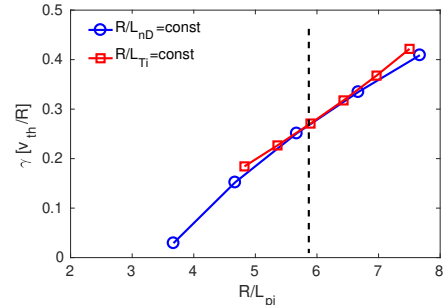


Figure 5: Growth rate as a function of the main ion pressure gradient for the most unstable mode, for the JET discharge 75225 at radial location $\rho = 0.15$ and $k_{\theta}\rho_i = 0.35$. Blue (open circle) curve for the case when the main ion density gradient (R/L_{nD}) is constant and the main ion temperature gradient (R/L_{Ti}) is varied, (red square) represents the case when the main ion temperature gradient is constant and the main ion density gradient is varied. The vertical (dotted) line indicates the experimental pressure gradient.

beta is then investigated. A magnetic shear \hat{s} scan is plotted in figure 6 (a), where the nominal value of \hat{s} is represented by a vertical dotted line. The mode growth rate decreases with increasing the absolute value of the magnetic shear until complete stabilisation. The low absolute value of the magnetic shear appears to be critical for the existence of unstable modes in the inner core of these hybrid plasmas. To illustrate the impact of the magnetic shear on the parallel mode structure, the real component of the perturbed electrostatic potential ϕ_r as a function of parallel coordinate χ for various values of the magnetic shear is shown in figure 6 (b). The mode extension along the field line gets reduced as the magnetic shear is increased. A plasma beta β_e scan is performed for three magnetic shear values in figure 7. At $\beta_e = 0$, $\gamma = 0$, hence there is no electrostatic instability present. Above the β_e threshold, the mode growth rate increases with beta and the mode frequency slowly decreases with beta. The threshold in beta increases with the magnetic shear. The low magnetic shear in

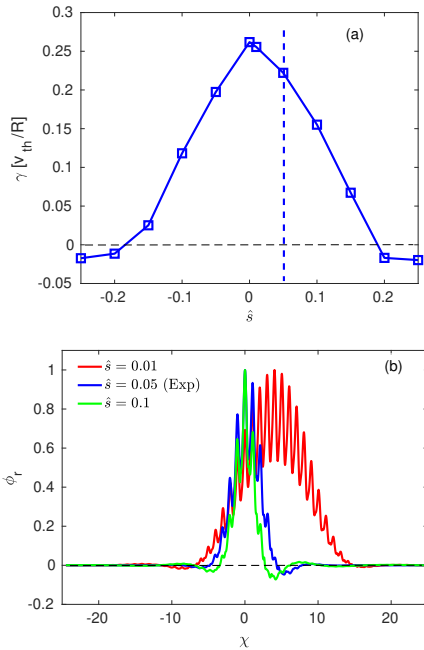


Figure 6: Linear growth rate as a function of \hat{s} (a) and parallel mode structure of ϕ as a function of parallel coordinates χ for various values of \hat{s} (b) for the most unstable mode, for the JET discharge 75225 at $\rho = 0.15$ and $k_{\theta}\rho_i = 0.35$.

the core of these hybrid plasmas results in a low β threshold. We now examine the impact of the pressure gradient β' on the local magnetic equilibrium, i.e. β' is varied keeping fixed the kinetic species gradients and the other magnetic equilibrium parameters. This is equivalent to an α scan for an $s - \alpha$ equilibrium, where $\alpha = -R_0 q^2 \beta'$. As seen from the comparison of Table 1 and 2, a β' scan differs from the self-consistent calculation of the magnetic equilibrium since in that case, the Shafranov shift is also modified. As shown in figure 8, increasing $|\beta'|$ has a strong stabilising impact on the mode. To finalise the parameter dependence study, the impact of T_e/T_i on the mode growth rate is investigated in figure 9, showing that an increase of T_e/T_i leads to an increase of the mode growth rate. The mode growth rate is found to be maximum around $q \sim 1$ (figures not shown) as pointed out in [13]. In comparison to the impact of magnetic shear, β or β' , the impact of the electron to ion temperature ratio T_e/T_i and safety factor q is smaller, but tends to favour the destabilisation of KBMs in electron heated plasmas with a q profile just above unity.

To summarise, the most unstable mode at $\rho = 0.15$ propagates in the ion magnetic drift direction with a real frequency much larger than the growth rate. The mode is driven by the ion pressure gradient and has an even (respectively odd) parity of eigenfunction in ϕ

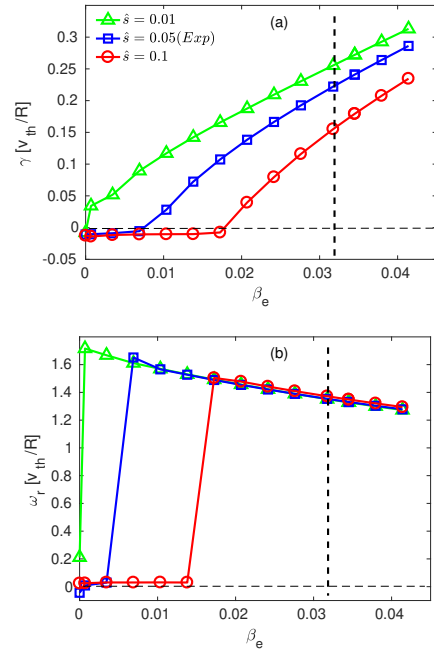


Figure 7: β_e scans for various values of \hat{s} , for the JET discharge 75225 at $\rho = 0.15$ and $k_{\theta}\rho_i = 0.35$. The top panel (a) shows the linear growth rates and the bottom panel (b) shows the corresponding frequencies for the most unstable mode. The blue curve is for experimental value of \hat{s} and vertical (dotted) line represents the corresponding nominal value of β_e (3.2%).

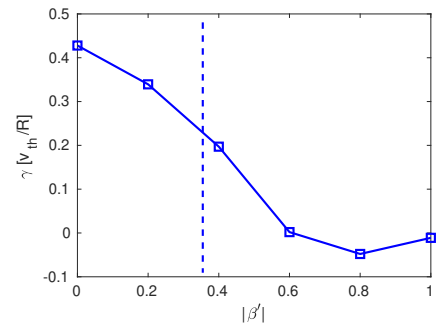


Figure 8: Growth rate as a function of $|\beta'|$, for the JET discharge 75225 at $\rho = 0.15$ and $k_{\theta}\rho_i = 0.35$. The vertical dotted line indicates the nominal value of $|\beta'|$.

(respectively A_{\parallel}) with an extended mode structure at low magnetic shear. Above a critical value β_e^{crit} , the mode is destabilised and its growth rate increases with β_e . The threshold in β_e increases with the magnetic shear which is reminiscent of the dependence of the MHD ballooning limit $\beta_{MHD}^{crit} \sim 0.6\hat{s}/[q_0^2(2R/L_n + R/L_{Ti} + R/L_{Te})]$ expected to approximately reproduce the dependences of β_e^{crit} for KBMs [27]. In addition, the mode is stabilised at high magnetic shear and high

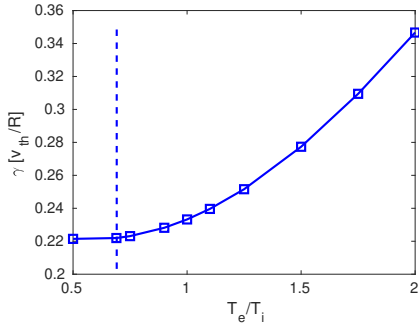


Figure 9: Growth rate as a function of T_e/T_i , for the JET discharge 75225 at $\rho = 0.15$ and $k_\theta \rho_i = 0.35$. The vertical dotted line indicates the nominal value of T_e/T_i .

$|\beta'| \propto \alpha$, as observed in [28] for KBMs. The stabilising effect of $|\beta'|$ is expected for ballooning modes as it reduces the curvature drift. All these features lead to the identification of this mode as a KBM, consistently with [13]. Note that due to the low magnetic shear value, the MHD ballooning limit is rather low $\beta_{MHD}^{crit} = 0.26\%$ (value at nominal parameters) and the threshold for the KBM is higher than the MHD ballooning limit, $\beta_e^{crit} > \beta_{MHD}^{crit}$, as observed at low R/L_{T_i} in [27].

We conclude this section by remarking that the destabilisation of KBMs at high beta, low magnetic shear and higher T_e/T_i ratio, suggests that these results are directly relevant for the prediction of inner core transport in ITER scenarios.

4. Non-linear simulations at $\rho = 0.15$

In this section, the level of turbulent transport driven by KBM modes for the JET 75225 discharge at $t = 6.0 - 6.5$ s and at $\rho = 0.15$ is investigated in the non-linear regime. The simulations are performed with $N_{mod} = 16$ binormal modes and $N_x = 509$ radial modes with a perpendicular box size of $[L_{radial}, L_{bi-normal}] = [126, 83]$ in units of ion Larmor radii. The poloidal wave vectors range from $k_\theta \rho_i = 0.1$ to 1.5 and the radial wave vectors extend up to $k_r \rho_i = \pm 12.3$. The high value of N_x was required to capture the elongated mode structures at low magnetic shear. A rather small time step of $\Delta t = 1.5 \times 10^{-4}$ (R_0/v_{thi}) was required in the simulations to guarantee numerical stability. The other simulation parameters are the same as described earlier in section 2: ion, electron and carbon as kinetic species, no kinetic fast ions, magnetic equilibrium with fast ion pressure, interspecies collisions with $Z_{eff} = 1.74$, no $E \times B$ shearing ($\gamma_E = 0$), parallel velocity gradient drive and inertial effects (Coriolis and centrifugal forces).

The heat and particle fluxes are normalized as:

$Q_{N,s} = \frac{Q_s^r}{n_s T_s \rho_*^2 v_{thi}}$; $\Gamma_{N,s} = \frac{\Gamma_s^r}{n_s \rho_*^2 v_{thi}}$, where $\rho_* = \rho_i/R_0$ is the normalized Larmor radius. The temporal evolution of the normalised non-linear electron and ion heat fluxes for the experimental input values of magnetic shear and plasma beta is presented in figure 10. The fluxes are decomposed into $E \times B$ (blue), magnetic flutter (red) and magnetic compression (green) contributions. The corresponding time averages are illustrated by horizontal dotted lines with the same colour coding as in the left figure. As seen here, the ion heat flux is dominated by the $E \times B$ contribution, with almost negligible contributions from the magnetic flutter and magnetic compression. For the electron heat flux, the $E \times B$ contribution is still dominant but the magnetic flutter also contributes significantly. Here, the most striking observation is that the magnetic flutter contribution in the non-linear phase has an opposite sign and is much larger than that in the linear phase. This point will be further investigated in the section dedicated to the quasi-linear modelling.

The time-averaged heat and particle fluxes are then shown as a function of β_e in figure 11. The value of $\rho_* = 0.0033$ was used for converting normalized fluxes to SI unit at $\rho = 0.15$. The time interval for the temporal average was from 120 and $300R_0/v_{thi}$ for all cases. Here, the total fluxes are indicated by a black line and the $E \times B$, magnetic flutter and magnetic compression contributions by coloured dotted lines blue, red and green. Heat fluxes for both the ion and the electron channels are observed to increase with increasing plasma beta. For ion heat transport, the fluxes are dominated by the $E \times B$ contribution. For electron heat transport, the magnetic flutter contribution increases with the plasma beta and becomes comparable to the $E \times B$ contribution at $\beta_e = 3.8\%$. The increase of heat and particle fluxes with β_e in figure 11 is qualitatively consistent with the linear destabilisation of the KBMs mode at higher beta seen in figure 7.

In figure 12, the fluxes dependence on the magnetic shear \hat{s} is illustrated in a two-point scan. The non-linear heat and particle fluxes for both the ion and the electron channel are reduced with increasing magnetic shear, which is also in qualitative agreement with the KBMs stabilisation observed at higher \hat{s} in the linear simulations of figure 6.

The quantitative comparison of the non-linear fluxes with the experimental values would require to include the impact of fast ions, which have been seen to be slightly stabilising linearly in section 3 and known to non-linearly stabilise ITG turbulence [14, 15, 29]. The impact of profile shearing effects, which by assumption is not included in the local approximation, has been shown to decrease the linear growth rate of KBMs

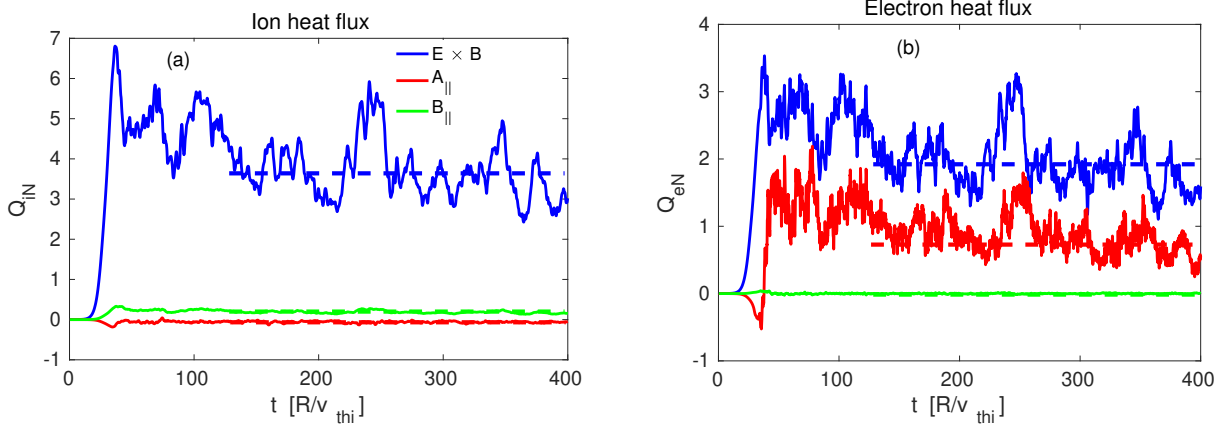


Figure 10: Time trace of nonlinear ion (a) and electron (b) normalised heat fluxes for the JET 75225 discharge at $\rho = 0.15$ for the reference case. The blue curve represents the $E \times B$ contribution to the fluxes, the red curve the magnetic flutter contribution (A_{\parallel}) and the green curve the magnetic contribution (B_{\parallel}).

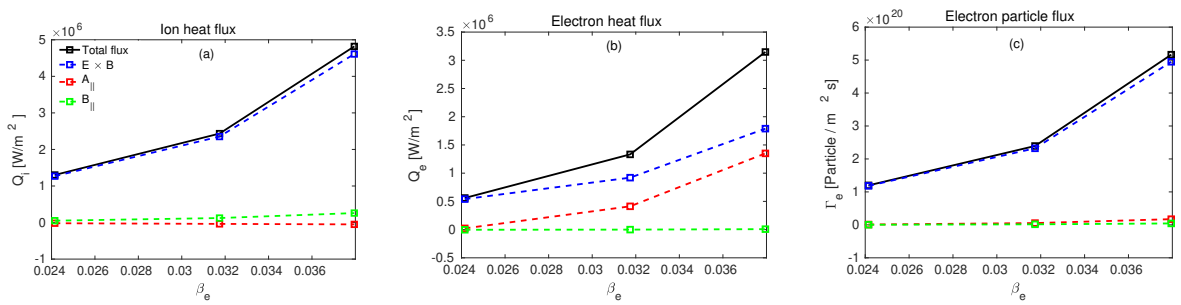


Figure 11: Nonlinear ion heat fluxes (a), electron heat fluxes (b) and electron particle fluxes (c) as a function of β_e , for the JET 75225 discharge at $\rho = 0.15$. The dotted blue curve represents the $E \times B$ contribution to the fluxes, the dotted red curve the magnetic flutter contribution, the dotted green curve the magnetic contribution and the solid black line the total fluxes.

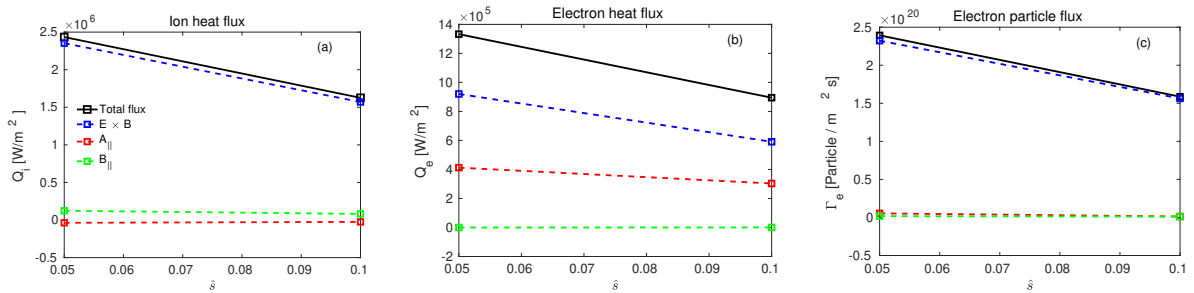


Figure 12: Nonlinear ion heat fluxes (a), electron heat fluxes (b) and electron particle fluxes (c) as a function of magnetic shear \hat{s} , for the JET 75225 discharge at $\rho = 0.15$. The dotted blue curve represents the $E \times B$ contribution to the fluxes, the dotted red curve the magnetic flutter contribution, the dotted green curve the magnetic contribution and the solid black line the total fluxes.

in hybrid H-modes [13] and should also be assessed. Finally, a scan in the main KBM drive, R/L_{T_i} and/or R/L_n , would also be required as mandatory in any comparison of gradient-driven simulation predictions with the experiments. Such a study is beyond the scope of the present work, but it is nevertheless interesting to

give the value of the experimental fluxes for reference. The electron and ion heat fluxes at $\rho = 0.15$, computed from power balance analysis with CRONOS in [14, 15], are $Q_e = 16 \text{ kW/m}^2$, $Q_i = 47 \text{ kW/m}^2$ and the particle flux is $\Gamma = 3.6 \times 10^{18} \text{ m}^{-2} \text{ s}^{-1}$. The neoclassical ion heat flux, $Q_i^{neo} = 13 \text{ kW/m}^2$, accounts for about a

third of the experimental ion heat flux. The computed turbulent fluxes are, therefore, almost two orders of magnitude larger than the experimental ones, which strongly invites to extend the study and at least perform a scan in the KBM drives (R/L_n and R/L_{Ti}).

5. Quasilinear Flux Modeling

Quasilinear models are used extensively for the prediction of heat, particle and momentum fluxes without the expensive numerical cost of nonlinear simulations [30, 31]. The purpose of the present section is to test the validity of standard quasi-linear models based on the non-linear simulations of section 4 featuring KBM turbulence in the inner core of the JET 75225 discharge at $t = 6.0 - 6.5$ s and $\rho = 0.15$.

5.1. Quasi-linear approximation

The quasi-linear approximation assumes that the phase difference between fluctuating fields (e.g. n and ϕ for the $E \times B$ particle flux) is similar in the linear and the non-linear regimes. This is usually observed of ITG and TEM turbulence and was more recently shown to also be valid for KBM turbulence [32]. When this approximation holds, the quasi-linear fluxes can be computed as [10, 33]:

$$Q_{s,E \times B}^{QL} = \sum_{k_r, k_\theta} Q_{s,E \times B}^N \mathcal{A}_{QL}^2 \quad (1)$$

$$Q_{s,A_{\parallel}}^{QL} = \sum_{k_r, k_\theta} Q_{s,A_{\parallel}}^N \mathcal{A}_{QL}^2 \quad (2)$$

where the first term on the right hand side is the flux normalized to the mode amplitude obtained in linear simulations, $Q_s^N = Q_s / \mathcal{A}_L^2$, and the second term is an approximation of the nonlinear saturation amplitude: $\mathcal{A}_{QL} \sim \mathcal{A}_{NL}$. In linear runs, the mode amplitude is defined as:

$$\mathcal{A}_L(k_r, k_\theta, t) = \sqrt{\int \int [|\phi|^2 + |A_{\parallel}|^2 + |B_{\parallel}|^2] d\chi} / \int d\chi \quad (3)$$

where χ is the parallel coordinate and the integral is performed over the full flux-tube domain, i.e. it includes several poloidal turns. In non-linear runs, an extra temporal average is added and the integral in the parallel direction is performed for one poloidal turn only:

$$\mathcal{A}_{NL}(k_r, k_\theta, t) = \sqrt{\frac{1}{\Delta t} \int \int [|\phi|^2 + |A_{\parallel}|^2 + |B_{\parallel}|^2] d\chi dt} \quad (4) \quad \mathcal{W}_n = C_n \mathcal{S}_k \max \left[\frac{\gamma}{\langle k_{\perp}^2 \rangle} \right] \frac{1}{k_{\theta} \rho_i^{max}} \quad (7)$$

with Δt the length of the interval used for the temporal average.

In most quasi-linear models, the linear fluxes are computed at $k_r \rho_i = 0$ only, which is what is done here. We verified in figure 13 that the KBM growth rate and

the linear fluxes vary very little with the radial wave vector.

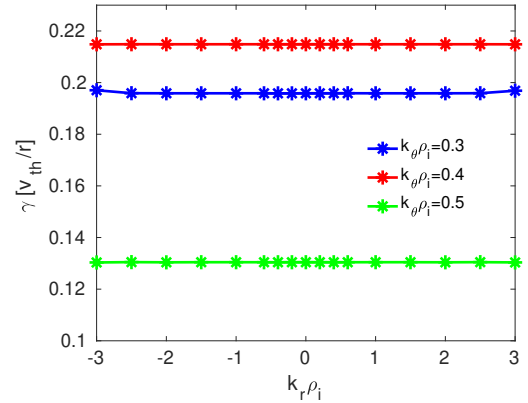


Figure 13: Linear growth rate as a function of radial wave vector ($k_r \rho_i$) for three different values of $k_\theta \rho_i$, for the JET discharge 75225 at $\rho = 0.15$. The blue curve corresponds to $k_\theta \rho_i = 0.3$, the red curve for $k_\theta \rho_i = 0.4$ and the green represents $k_\theta \rho_i = 0.5$.

5.1.1. Mixing length model : A very common choice for the quasi-linear model is to define the saturated mode amplitude based on a mixing length estimate [33]:

$$W_1 = C_1 \max \left[\frac{\gamma}{\langle k_{\perp}^2 \rangle}, 0 \right] \quad (5)$$

and assume $\mathcal{A}_{QL}^2 = W_1$ to compute the quasi-linear fluxes using Eq. (1). Here, $\langle k_{\perp}^2 \rangle$ is an effective perpendicular wavevector defined as:

$$\langle k_{\perp}^2 \rangle = \frac{\int k_{\perp}(s)^2 |\phi|^2 d\chi}{\int |\phi|^2 d\chi} \quad (6)$$

where the integral is performed along the whole flux tube. The main drawback of this model is that linearly stable modes will never contribute to the quasi-linear fluxes. As we will see, in the present case, this prevents from capturing the magnetic flutter fluxes at low $k_\theta \rho_i$.

5.1.2. QuaLiKiz model : Another widely used quasi-linear model is the one integrated in QuaLiKiz [10, 34]. In this model, the saturated mode amplitude is approximated by:

$$\mathcal{W}_n = C_n \mathcal{S}_k \max \left[\frac{\gamma}{\langle k_{\perp}^2 \rangle} \right] \frac{1}{k_{\theta} \rho_i^{max}} \quad (7)$$

with

$$\mathcal{S}_k = \left(\frac{k_{\theta} \rho_i}{k_{\theta} \rho_i^{max}} \right)^{x_n} \quad \text{for} \quad k_{\theta} \rho_i < k_{\theta} \rho_i^{max} \quad (8)$$

$$\mathcal{S}_k = \left(\frac{k_{\theta} \rho_i}{k_{\theta} \rho_i^{max}} \right)^{-3} \quad \text{for} \quad k_{\theta} \rho_i > k_{\theta} \rho_i^{max} \quad (9)$$

where the maximum of $\gamma/\langle k_{\perp}^2 \rangle$ is taken over the $k_{\theta\rho_i}$ spectrum and $k_{\theta\rho_i}^{max}$ is the wave vector at which this maximum is reached. Here, we will test two different spectral shapes: W_2 and W_3 with $x_2 = 1$ and $x_3 = 2$, respectively, to highlight the sensitivity of the magnetic flutter fluxes to the spectral rule used at low $k_{\theta\rho_i}$. W_2 is the present choice in QuaLiKiz. Note that the QuaLiKiz model includes other-dimensional terms that are absorbed in the C_n factor since they do not vary in the present study. The QuaLiKiz model also offers the possibility to account for the contributions of several eigenmodes per wavevector. In the present work, we consider only the contribution from the most unstable mode.

The constants C_1 , C_2 and C_3 are unique and set by matching the ion heat flux in the non-linear simulation performed at nominal parameters.

5.2. Linear heat and particle fluxes

The linear heat and particle fluxes normalised to the mode amplitude are presented in figure 14 as a function of $k_{\theta\rho_i}$ for the nominal parameters at $\rho = 0.15$. The flux contribution due to magnetic flutter and compression part for particle and heat (electrons, ions) is negligible compared to the $E \times B$ part, except at low $k_{\theta\rho_i}$ modes. At $k_{\theta\rho_i} = 0.1$, the electron heat flux from magnetic flutter contributions is about 9.4 (this point cannot be seen in the figure 14 (b)) and largely exceeds the $E \times B$ contribution. The large (normalised) electron heat flux from magnetic flutter is observed in the spectral region where micro-tearing modes are identified in figure 2. These micro-tearing modes are linearly stable ($\gamma < 0$) but are nevertheless the modes with the largest growth rate at low $k_{\theta\rho_i}$ values.

5.3. Comparison of quasi-linear and non-linear spectra

The non-linear $k_{\theta\rho_i}$ spectra of ϕ and A_{\parallel} are compared to the various quasi-linear spectra introduced above for different plasma beta and magnetic shear in figures 15 and 16. Here, figure 15 (a) is for $\beta_e = 2.4\%$, (b) for $\beta_e = 3.2\%$, (c) corresponds to $\beta_e = 3.8\%$ at nominal magnetic shear ($\hat{s} = 0.05$) and (d) is for higher magnetic shear $\hat{s} = 0.1$ at nominal beta ($\beta_e = 3.2\%$). The values of $\mathcal{A}_{A_{\parallel},NL}^2$ are much lower than that of $\mathcal{A}_{\phi,NL}^2$, but the ϕ and A_{\parallel} non-linear spectra have a very similar shape. At higher beta, the peak of non-linear spectra are shifted towards low $k_{\theta\rho_i}$ values, as previously observed in [35]. Note that the non-linear spectra are much less peaked than those observed in [32] for the Cyclone Base Case at $R/L_{T_e} = 0$ and are more typical of those observed for ITG turbulence. The quasi-linear spectra are normalised to the peak of the non-linear spectrum to focus on how accurately

they reproduce the shape of the non-linear spectra. As anticipated, the standard mixing length model does not capture the finite amplitude of the fields for $k_{\theta\rho_i} < 0.3$ since all linear modes are stable in this region. The QuaLiKiz-like model performs much better to this respect, especially the W_3 variant. All models fail to capture the variation of the spectral width and peak location with β .

5.4. Comparison of quasi-linear fluxes with non-linear simulations

The quasilinear heat, particle and momentum fluxes obtained with the quasilinear models W_1 , W_2 and W_3 are now compared with the non-linear fluxes, using the same $k_{\theta\rho_i}$ grid as in the non-linear simulations to compute the normalised linear fluxes. A scalar multiplication factor of $C_1 = 12.4$, $C_2 = 4.24$ and $C_3 = 4.32$ is used to match the computed quasilinear ion heat flux with the non-linear simulations at $\beta_e = 3.2\%$.

5.4.1. $E \times B$ fluxes The corresponding $E \times B$ heat, particle and momentum fluxes are plotted in figure 17 for the beta scan. All quasi-linear models yield comparable results for the $E \times B$ part of the electron and ion heat fluxes. The general trend of increasing $E \times B$ heat flux with β is captured but the steeper increase at high β is underestimated by 20 to 25% by all models. The same situation is observed for the $E \times B$ particle and momentum fluxes, i.e. the increase of the flux with β is well captured at low β but underestimated by some 25% at $\beta_e = 3.8\%$. For the momentum flux, the W_3 model performs significantly better than the others do. The comparison is then extended to the magnetic shear scan in figure 18. The quasi-linear heat, particle and momentum $E \times B$ fluxes decrease with a higher absolute value of magnetic shear, in qualitative agreement with the non-linear results. Quantitatively, the mixing length model W_1 perform the worst and underestimates the ion heat flux found with GKW non-linear results by $\sim 42\%$ and electron heat flux by $\sim 53\%$ at high magnetic shear $\hat{s} = 0.1$. The best results are obtained with the W_3 model which underestimates the ion heat flux by $\sim 14\%$ whereas it is in good agreement for the electron heat flux at higher magnetic shear. The same trend is obtained for the particle and momentum flux, with W_3 performing significantly better than the other models.

5.5. Magnetic flutter fluxes

As seen in figure 11 and 12, the only non-negligible magnetic flutter contribution is to the electron heat flux. We will therefore focus on this channel for the comparison with the quasi-linear models. The

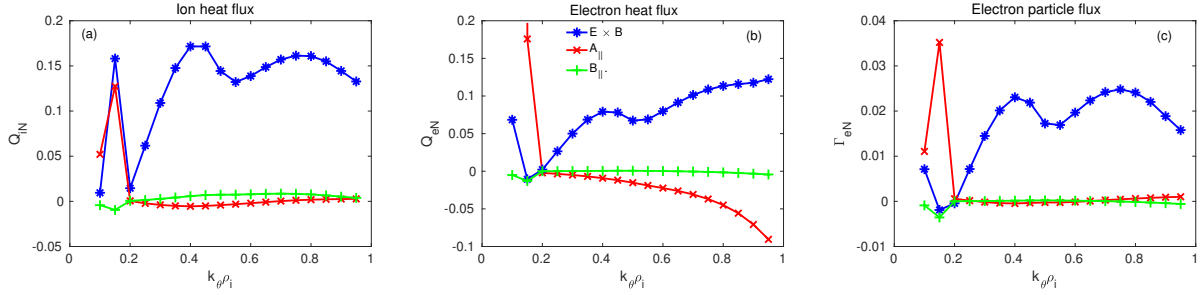


Figure 14: Linear ion (a), electron heat fluxes (b), and particle fluxes (c) normalised with the mode amplitude as a function of $k_{\theta}\rho_i$, for the JET 75225 discharge at $\rho = 0.15$. The blue (*) curve corresponds to flux contribution due to $E \times B$, the red (x) for magnetic flutter and green (+) for magnetic compression part.

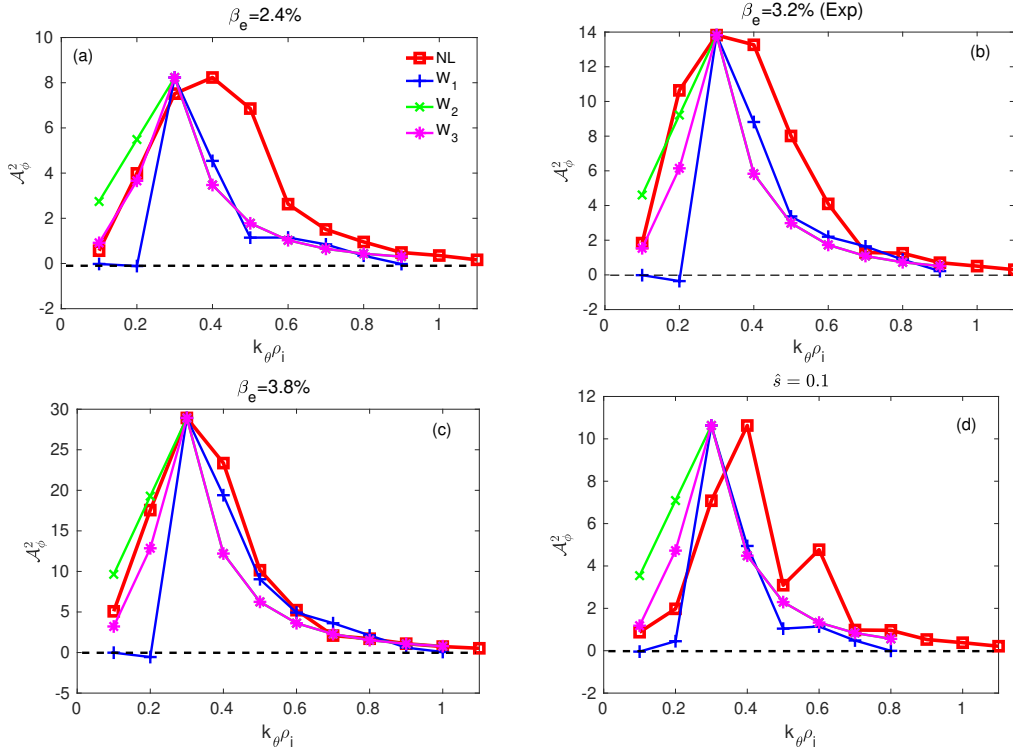


Figure 15: Normalized quasilinear spectra and GKW non-linear saturated electric potential for different plasma beta $\beta_e = 2.4\%$ (a), $\beta_e = 3.2\%$ (b), $\beta_e = 3.8\%$ (c) with nominal magnetic shear ($\hat{s} = 0.05$), and for higher magnetic shear $\hat{s} = 0.1$ at nominal plasma beta ($\beta_e = 3.2\%$) (d) as function of $k_{\theta}\rho_i$, for the JET 75225 discharge at $\rho = 0.15$. The quasi-linear spectra are normalized to the maximum of the nonlinear ones. The red curve (square) corresponds to nonlinear, the blue (+) to the quasi-linear model W_1 , the green (x) for W_2 and the magenta (*) for W_3 .

fluxes obtained with the W_1 , W_2 and W_3 models are compared to the non-linear fluxes in figure 19. The mixing length model W_1 strongly underestimates the magnetic flutter contribution, as anticipated, since it cannot capture the contribution from the linearly stable micro-tearing modes at $k_{\theta}\rho_i < 0.2$. In contrast, the W_2 and W_3 models strongly overestimate the magnetic flutter heat flux. The factor of 3 difference between the electron heat flux predictions of the W_2

and W_3 models highlights the extreme sensitivity to the model amplitude for the lower end of the $k_{\theta}\rho_i$ spectrum.

To better understand this discrepancy, the ratio of the A_{\parallel} fluctuations amplitude to the total fluctuation amplitude is shown in figure 20 as a function of $k_{\theta}\rho_i$ for linear and non-linear simulations. For $k_{\theta}\rho_i > 0.2$, this ratio is observed to be comparable in linear and non-linear simulations, but at $k_{\theta}\rho_i = 0.1$ the linear ratio

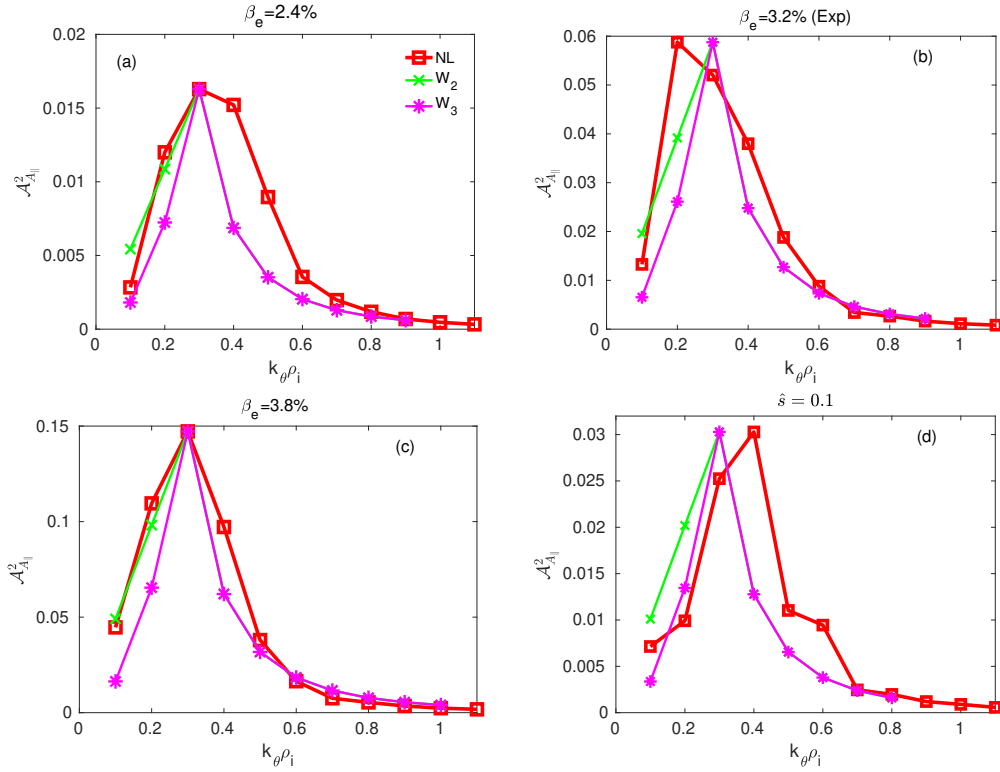


Figure 16: Normalized quasilinear spectra and GKW non-linear saturated vector potential for different plasma beta $\beta_e = 2.4\%$ (a), $\beta_e = 3.2\%$ (b), $\beta_e = 3.8\%$ (c) with nominal magnetic shear, and for higher magnetic shear $\hat{s} = 0.1$ at nominal plasma beta (d) as function of $k_{\theta}\rho_i$, for the JET discharge 75225 at $\rho = 0.15$. The quasi-linear spectra are normalized to the maximum of the nonlinear ones. The red curve (square) corresponds to nonlinear, the blue (+) to the quasi-linear model W_1 , the green (\times) for W_2 and the magenta ($*$) for W_3 .

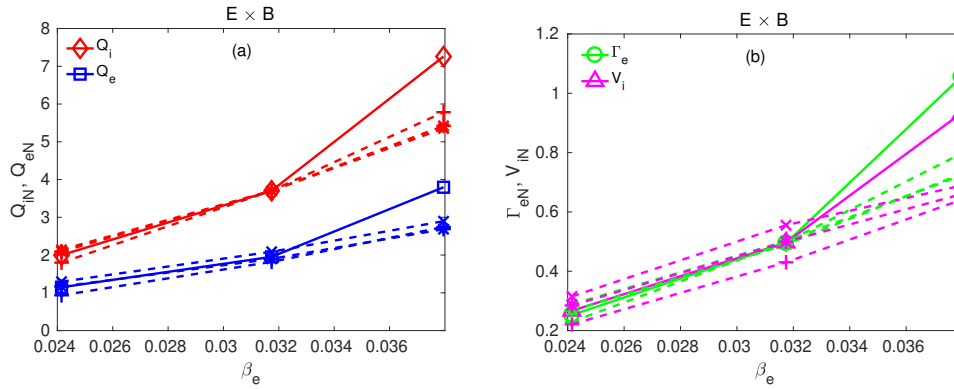


Figure 17: $E \times B$ ion and electron heat fluxes (a) and particle and ion momentum flux (b) as a function of β_e , for the JET 75225 discharge at $\rho = 0.15$. The solid lines are for the non-linear results and the dashed lines for the quasilinear models. The plus signs + corresponds to the QL model W_1 , the crosses \times are for W_2 and the star $*$ are for W_3 .

is more than 10 times larger than the non-linear one. Linearly, the ratio $\mathcal{A}_{A_{||}}^2/\mathcal{A}^2$ at low $k_{\theta}\rho_i$ is governed by the most unstable mode, i.e. micro-tearing modes in the present case. Since these modes are linearly stable the evolution of their amplitude tends to be dominated by the non-linear interactions, which results in a much

smaller value of $\mathcal{A}_{A_{||}}^2/\mathcal{A}^2$ at $k_{\theta}\rho_i = 0.1$ in the non-linear regime.

In an attempt to capture this effect in the QuaLiKiz-like quasi-linear model, we introduce an extra normalisation of the magnetic flutter fluxes. We

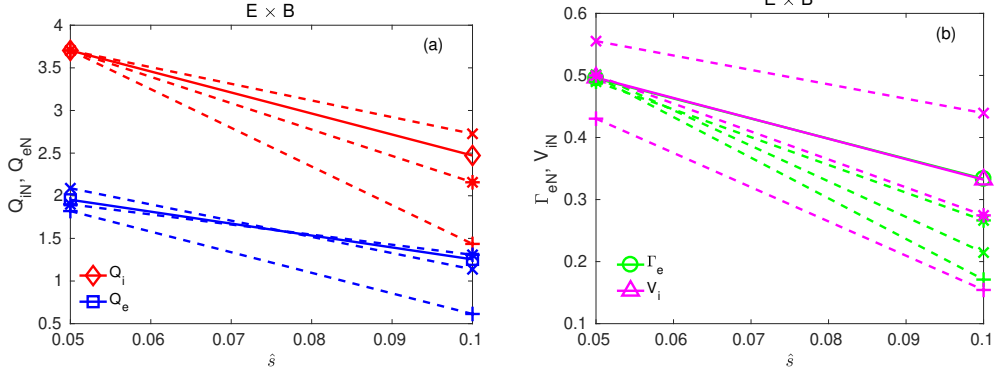


Figure 18: $E \times B$ ion and electron heat fluxes (a) and particle and ion momentum flux (b) as a function of the magnetic shear \hat{s} , for the JET 75225 discharge at $\rho = 0.15$. The solid lines are for the non-linear results and the dashed lines for the quasilinear models. The plus signs + corresponds to the QL model W_1 , the crosses \times are for W_2 and the star * are for W_3 .

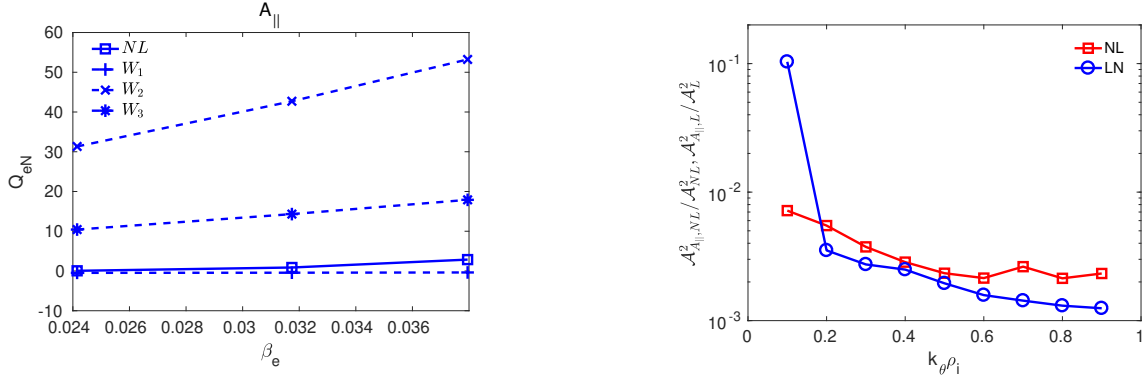


Figure 19: Magnetic flutter electron heat flux as a function of β_e , for the JET 75225 discharge at $\rho = 0.15$. The solid lines are the non-linear results and the dashed lines are for the quasilinear models. The plus signs + corresponds to QL weight W_1 , the crosses \times are for W_2 and the star * are for W_3 .

first assume that:

$$\frac{\mathcal{A}_{A_{\parallel},NL}}{\mathcal{A}_{NL}} \sim \frac{\mathcal{A}_{A_{\parallel},L}(k_{\theta}\rho_i^{max})}{\mathcal{A}_L(k_{\theta}\rho_i^{max})} \quad (10)$$

and then, introduce the following quantity:

$$A_{\parallel}^{ratio} = \frac{\mathcal{A}_L(k_{\theta}\rho_i)}{\mathcal{A}_{A_{\parallel},L}(k_{\theta}\rho_i)} \frac{\mathcal{A}_{A_{\parallel},L}(k_{\theta}\rho_i^{max})}{\mathcal{A}_L(k_{\theta}\rho_i^{max})} \quad (11)$$

that is used to renormalise the amplitude of A_{\parallel} in the magnetic flutter fluxes based on the assumption in Eq. (10):

$$Q_{s,A_{\parallel}}^{QL} = \sum_{k_{\theta}} Q_{s,A_{\parallel}}^N \mathcal{A}_{QL}^2 A_{\parallel}^{ratio} \quad (12)$$

This model will be referred as W_2^* and W_3^* and is compared to the non-linear results in figure 21. The renormalisation of A_{\parallel} in the linear magnetic flutter

Figure 20: Ratio of the A_{\parallel} fluctuations amplitude, $\mathcal{A}_{A_{\parallel},NL}^2/\mathcal{A}_{NL}^2, \mathcal{A}_{A_{\parallel},L}^2/\mathcal{A}_L^2$ as a function of $k_{\theta}\rho_i$ in linear and non-linear simulations, for JET 75225 at $\rho = 0.15$.

fluxes makes the prediction of the QuaLiKiz-like model much closer to the values of the fluxes obtained in the non-linear simulations, in particular for W_3^* . The extreme sensitivity to the assumption used for the low $k_{\theta}\rho_i$ part of the spectrum is again highlighted by comparing W_2^* and W_3^* : more than a factor of three difference on the magnetic flutter electron heat flux can be obtained with a modest change in the quasi-linear spectrum. The non-linear excitation of sub-dominant MTMs and their contribution to magnetic flutter transport is an area of research on its own [36,37] and it is clear that more work is required to accurately predict the magnetic flutter fluxes in a quasi-linear model. It is nevertheless encouraging to see that once the saturated level of A_{\parallel} is captured, standard quasi-linear models predictions are of the right order of magnitude compared to non-linear results. To summarise this section, the quasi-linear ion and electron heat fluxes

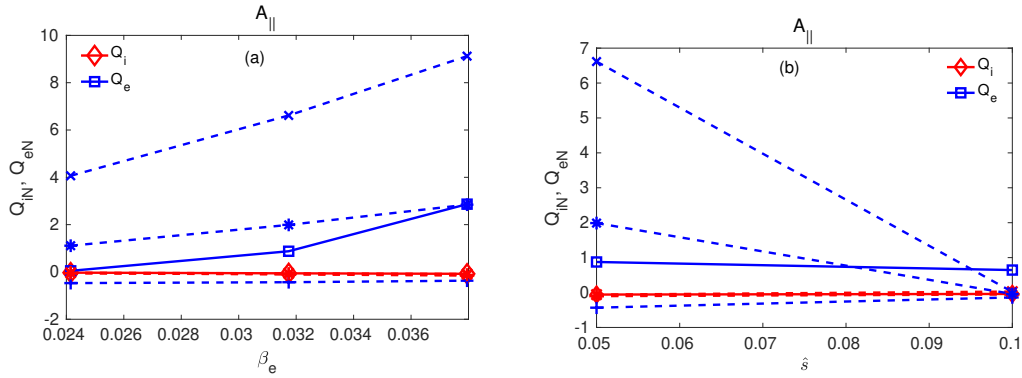


Figure 21: Magnetic flutter ion and electron heat fluxes as a function of β_e (a) and magnetic shear (b) for the JET 75225 discharge at $\rho = 0.15$. The solid lines are the non-linear results and the dashed lines are for the quasi-linear models. The plus signs + corresponds to the model W_1 , the crosses \times are for W_2^* and the star * are for W_3^* .

and particle fluxes estimation for three different QL models are found in reasonable agreement with non-linear fluxes amplitude for the $E \times B$ contribution with some departure at higher beta and high magnetic shear, especially for the basic mixing length model (W_1). For the magnetic flutter contribution to the electron heat flux, which represents about half of the total $E \times B$ electron heat flux, capturing the contribution of linearly stable micro-tearing modes excited in the non-linear regime is essential. This proves to be a difficult exercise, extremely sensitive to the exact value of the saturated A_{\parallel} values at low $k_{\theta}\rho_i$. The QuaLiKiz-like mixing length model (W_3^*) yields the best results, even though further improvements would be desirable.

6. Conclusions

To better understand turbulent transport and to test the quasi-linear approximation in the central region of tokamak plasmas, close to the magnetic axis, a linear and non-linear gyro-kinetic investigation has been carried out for JET high- β MHD-free hybrid H-mode discharge 75225 in the time interval $t=6.0 - 6.5$ s at $\rho = 0.15$ using the gyro-kinetic code GWK in the local approximation. It is found that in spite of lower gradients close to the magnetic axis, the plasma is linearly unstable and that turbulent transport is non-negligible in the central part. The pressure-driven instability arising in this region has been identified as a Kinetic Ballooning Mode (KBM). It has an extended poloidal mode structure due to the low magnetic shear. The low magnetic shear and high plasma beta are the main parameters responsible for the destabilisation of KBM in this region. The KBM is found to be the most unstable mode in the inner core plasma region up to $\rho = 0.33$, whereas at mid and outer

radius, $\rho > 0.4$, ITG is the dominant instability. The excitation of KBMs is also seen non-linearly where the non-linear fluxes increase with higher beta and lower $|\hat{s}|$ consistently with linear results. Non-linearly, the $E \times B$ contribution to the ion heat flux is found to be dominant. For the electron heat flux, a sizeable contribution from the magnetic flutter flux is observed. This contribution arises from stable micro-tearing modes at $k_{\theta}\rho_i < 0.2$ that are excited non-linearly. We have also tested the validity of various quasi-linear models employed in standard quasi-linear codes. At $\rho = 0.15$, we found that the quasi-linear fluxes estimates are in agreement with non-linear fluxes for the $E \times B$ contributions with some departure at high beta. However, these models fail to capture the magnetic flutter contribution to the electron heat fluxes due to the non-linearly excited micro-tearing modes. An extension of the model used in QuaLiKiz is shown to improve the description of the magnetic flutter contribution, even though further work would be required to obtain a robust model.

A sizeable level of turbulent diffusion transport in the inner plasma core is favourable to avoid W neoclassical accumulation, although by flattening the core particle peaking, it is unfavourable for the fusion gain. Turbulent diffusive-like particle transport can mitigate the neoclassical inward pinch of W in the inner core and help in preventing W accumulation. This mechanism could be particularly relevant for ITER where the level of neoclassical transport to overcome is low and the plasma beta for high Q operation is high. To test this mechanism, the present gyrokinetic analysis has been extended to the ITER conventional H-mode scenario in DT with 15 MA plasma current and $Q=10$. Reference profiles for this case were obtained from ASTRA simulations using a scaling based transport model for the core and with

EPED1+SOLPS pedestal for the H-mode $Hy2$, 98 = 1 [38]. It is found that KBM is also unstable for this predicted ITER H-mode case. The next steps of this work are to expand this evaluation to other ITER low Q scenarios, such as the $Q = 5$ steady-state one, and predict the impact of the profile flattening induced by KBM turbulence on the fusion gain and W accumulation.

Acknowledgements

The authors would like to thank A. Ho for providing GPR fits, J. Citrin, M.J. Pueschel and D. Zarzoso for fruitful discussions.

Part of this work has been carried out within the framework of the EUROfusion Consortium and has received funding from the Euratom research and training programme 2014-2018 and 2019-2020 under grant agreement No 633053. The views and opinions expressed herein do not necessarily reflect those of the European Commission.

The views and opinions expressed herein do not necessarily reflect those of the ITER Organization.

This work was also conducted under the auspices of the ITPA Topical Group on Transport & Confinement. The authors acknowledge access to the EUROfusion High-Performance Computer (Marconi–Fusion) through EUROfusion. Centre de Calcul Intensif d’Aix-Marseille is acknowledged for granting access to its high-performance computing resources.

References

- [1] Rion A Causey. Hydrogen isotope retention and recycling in fusion reactor plasma-facing components. *Journal of Nuclear Materials*, 300(2):91 – 117, 2002.
- [2] H Bolt, V Barabash, W Krauss, J Linke, R Neu, S Suzuki, N Yoshida, and ASDEX Upgrade Team. Materials for the plasma-facing components of fusion reactors. *Journal of Nuclear Materials*, 329-333:66 – 73, 2004. Proceedings of the 11th International Conference on Fusion Reactor Materials (ICFRM-11).
- [3] V. Philipps. Tungsten as material for plasma-facing components in fusion devices. *Journal of Nuclear Materials*, 415(1, Supplement):S2 – S9, 2011. Proceedings of the 19th International Conference on Plasma-Surface Interactions in Controlled Fusion.
- [4] A Kallenbach, R Neu, R Dux, H-U Fahrbach, J C Fuchs, L Giannone, O Gruber, A Herrmann, P T Lang, B Lipschultz, C F Maggi, J Neuhauser, V Philipps, T Pütterich, V Rohde, J Roth, G Sergienko, A Sips, and ASDEX Upgrade Team. Tokamak operation with high-z plasma facing components. *Plasma Physics and Controlled Fusion*, 47(12B):B207–B222, 2005.
- [5] T Pütterich, R Dux, R Neu, M Bernert, M N A Beurskens, V Bobkov, S Brezinsek, C Challis, J W Coenen, I Coffey, A Czarnecka, C Giroud, P Jacquet, E Joffrin, A Kallenbach, M Lehnen, E Lerche, E de la Luna, S Marsen, G Matthews, M-L Mayoral, R M McDermott, A Meigs, J Mlynar, M Sertoli, G van Rooij, and and. Observations on the w-transport in the core plasma of JET and ASDEX upgrade. *Plasma Physics and Controlled Fusion*, 55(12):124036, 2013.
- [6] C. Angioni, P. Mantica, T. Pütterich, M. Valisa, M. Baruzzo, E.A. Belli, P. Belo, F.J. Casson, C. Challis, P. Drewelow, C. Giroud, N. Hawkes, T.C. Hender, J. Hobirk, T. Koskela, L. Lauro Taroni, C.F. Maggi, J. Mlynar, T. Odstrcil, M.L. Reinke, and M. Romanelli and. Tungsten transport in JET h-mode plasmas in hybrid scenario, experimental observations and modelling. *Nuclear Fusion*, 54(8):083028, 2014.
- [7] F J Casson, C Angioni, E A Belli, R Bilato, P Mantica, T Odstrcil, T Pütterich, M Valisa, L Garzotti, C Giroud, J Hobirk, C F Maggi, J Mlynar, and M L Reinke. Theoretical description of heavy impurity transport and its application to the modelling of tungsten in JET and ASDEX upgrade. *Plasma Physics and Controlled Fusion*, 57(1):014031, nov 2014.
- [8] Loarte et al 2016. *Evaluation of tungsten transport and concentration control in iter scenarios Preprint: 2016 IAEA Fusion Energy Conference, Kyoto, Japan [ppc/2-1]*. <https://nucleus.iaea.org/sites/fusionportal/Shared>
- [9] F Köchl, A Loarte, E de la Luna, V Parail, G Corrigan, D Harting, I Nunes, C Reux, F G Rimini, A Polevoi, and M Romanelli and. W transport and accumulation control in the termination phase of JET h-mode discharges and implications for ITER. *Plasma Physics and Controlled Fusion*, 60(7):074008, jun 2018.
- [10] C. Bourdelle, X. Garbet, F. Imbeaux, A. Casati, N. Dubuit, R. Guirlet, and T. Parisot. A new gyrokinetic quasilinear transport model applied to particle transport in tokamak plasmas. *Physics of Plasmas*, 14(11):112501, 2007.
- [11] G. M. Staebler, J. E. Kinsey, and R. E. Waltz. A theory-based transport model with comprehensive physics. *Physics of Plasmas*, 14(5):055909, 2007.
- [12] A.G. Peeters, Y. Camenen, F.J. Casson, W.A. Hornsby, A.P. Snodin, D. Strintzi, and G. Szepesi. The nonlinear gyro-kinetic flux tube code gkw. *Computer Physics Communications*, 180(12):2650 – 2672, 2009.
- [13] S. Moradi, I. Pusztai, I. Voitsekhovitch, L. Garzotti, C. Bourdelle, M.J. Pueschel, I. Lupelli, and M. Romanelli and. Core micro-instability analysis of JET hybrid and baseline discharges with carbon wall. *Nuclear Fusion*, 54(12):123016, 2014.
- [14] J Citrin, J Garcia, T Gorler, F Jenko, P Mantica, D Told, C Bourdelle, D R Hatch, G M D Hogewij, T Johnson, M J Pueschel, and M Schneider. Electromagnetic stabilization of tokamak microturbulence in a high- β regime. *Plasma Physics and Controlled Fusion*, 57(1):014032, 2015.
- [15] J. Garcia, C. Challis, J. Citrin, H. Doerk, G. Giruzzi, T. Görler, F. Jenko, and P. Maget and. Key impact of finite-beta and fast ions in core and edge tokamak regions for the transition to advanced scenarios. *Nuclear Fusion*, 55(5):053007, apr 2015.
- [16] J Hobirk, F Imbeaux, F Crisanti, P Buratti, C D Challis, E Joffrin, B Alper, Y Andrew, P Beaumont, M Beurskens, A Boboc, A Botrugno, M Brix, G Calabro, I Coffey, S Conroy, O Ford, D Frigione, J Garcia, C Giroud, N C Hawkes, D Howell, I Jenkins, D Keeling, M Kempenaars, H Leggate, P Lotte, E de la Luna, G P Maddison, P Mantica, C Mazzotta, D C McDonald, A Meigs, I Nunes, E Rachlew, F Rimini, M Schneider, A C C Sips, J K Stober, W Studholme, T Tala, M Tsalias, I Voitsekhovitch, and P C de Vries. Improved confinement in JET hybrid discharges. *Plasma Physics and Controlled Fusion*, 54(9):095001, 2012.
- [17] J. Garcia and G. Giruzzi and. On the different physical mechanisms for accessing hybrid scenarios on JET. *Nuclear Fusion*, 53(4):043023, 2013.
- [18] A. Ho, J. Citrin, F. Auriemma, C. Bourdelle, F.J. Casson,

- Hyun-Tae Kim, P. Manas, G. Szepesi, and H. Weisen and. Application of gaussian process regression to plasma turbulent transport model validation via integrated modelling. *Nuclear Fusion*, 59(5):056007, 2019.
- [19] A. Di Siena, T. Görler, H. Doerk, R. Bilato, J. Citrin, T. Johnson, M. Schneider, and E. Poli. Non-maxwellian fast particle effects in gyrokinetic gene simulations. *Physics of Plasmas*, 25(4):042304, 2018.
- [20] R. L. Miller, M. S. Chu, J. M. Greene, Y. R. Lin-Liu, and R. E. Waltz. Noncircular, finite aspect ratio, local equilibrium model. *Physics of Plasmas*, 5(4):973–978, 1998.
- [21] H. Lütjens, A. Bondeson, and O. Sauter. The chease code for toroidal mhd equilibria. *Computer Physics Communications*, 97(3):219 – 260, 1996.
- [22] H. Doerk, F. Jenko, T. Görler, D. Told, M. J. Pueschel, and D. R. Hatch. Gyrokinetic prediction of microtearing turbulence in standard tokamaks. *Physics of Plasmas*, 19(5):055907, 2012.
- [23] C. Bourdelle, W. Dorland, X. Garbet, G. W. Hammett, M. Kotschenreuther, G. Rewoldt, and E. J. Synakowski. Stabilizing impact of high gradient of β on microturbulence. *Physics of Plasmas*, 10(7):2881–2887, 2003.
- [24] C.D. Challis, J.G. Cordey, H. Hamnén, P.M. Stubberfield, J.P. Christiansen, E. Lazzaro, D.G. Muir, D. Stork, and E. Thompson. Non-inductively driven currents in JET. *Nuclear Fusion*, 29(4):563–570, apr 1989.
- [25] M. Schneider, L.-G. Eriksson, I. Jenkins, J.F. Artaud, V. Basiuk, F. Imbeaux, T. Oikawa, and and. Simulation of the neutral beam deposition within integrated tokamak modelling frameworks. *Nuclear Fusion*, 51(6):063019, may 2011.
- [26] N Kumar, Y Camenen, C Bourdelle, S Benkadda, A Loarte, AR Polevoi, and JET Contributors. *Linear stability of the inner core of JET plasmas using gyrokinetic simulations. 46th EPS Conference on Plasma Physics, (EPS 2019), Milan, Italy.* <http://ocs.ciemat.es/EPS2019PAP/pdf/P5.1076.pdf>.
- [27] M. J. Pueschel, M. Kammerer, and F. Jenko. Gyrokinetic turbulence simulations at high plasma beta. *Physics of Plasmas*, 15(10):102310, 2008.
- [28] A. Hirose, L. Zhang, and M. Elia. Erratum: “ion temperature gradient-driven ballooning mode in tokamaks” [phys. plasmas 2, 859 (1995)]. *Physics of Plasmas*, 3(1):439–439, 1996.
- [29] J. Citrin, F. Jenko, P. Mantica, D. Told, C. Bourdelle, J. Garcia, J. W. Haverkort, G. M. D. Hogeweij, T. Johnson, and M. J. Pueschel. Nonlinear stabilization of tokamak microturbulence by fast ions. *Phys. Rev. Lett.*, 111:155001, Oct 2013.
- [30] A. Casati, C. Bourdelle, X. Garbet, F. Imbeaux, J. Candy, F. Clairet, G. Dif-Pradalier, G. Falchetto, T. Gerbaud, V. Grandgirard, Ö.D. Gürçan, P. Hennequin, J. Kinsey, M. Ottaviani, R. Sabot, Y. Sarazin, L. Vermare, and R.E. Waltz. Validating a quasi-linear transport model versus nonlinear simulations. *Nuclear Fusion*, 49(8):085012, jul 2009.
- [31] J. E. Kinsey, G. M. Staebler, and R. E. Waltz. The first transport code simulations using the trapped gyro-landau-fluid model. *Physics of Plasmas*, 15(5):055908, 2008.
- [32] S. Maeyama, A. Ishizawa, T.-H. Watanabe, M. Nakata, N. Miyato, M. Yagi, and Y. Idomura. Comparison between kinetic-ballooning-mode-driven turbulence and ion-temperature-gradient-driven turbulence. *Physics of Plasmas*, 21(5):052301, 2014.
- [33] Tilman Dannert and Frank Jenko. Gyrokinetic simulation of collisionless trapped-electron mode turbulence. *Physics of Plasmas*, 12(7):072309, 2005.
- [34] J. Citrin. Qualikiz saturation rule. https://gitlab.com/qualikiz-group/QualiKiz-documents/-/blob/master/reports/saturation_rule.pdf.
- [35] J. Candy. Beta scaling of transport in microturbulence simulations. *Physics of Plasmas*, 12(7):072307, 2005.
- [36] D. R. Hatch, M. J. Pueschel, F. Jenko, W. M. Nevins, P. W. Terry, and H. Doerk. Origin of magnetic stochasticity and transport in plasma microturbulence. *Phys. Rev. Lett.*, 108:235002, Jun 2012.
- [37] D. R. Hatch, M. J. Pueschel, F. Jenko, W. M. Nevins, P. W. Terry, and H. Doerk. Magnetic stochasticity and transport due to nonlinearly excited subdominant microtearing modes. *Physics of Plasmas*, 20(1):012307, 2013.
- [38] A.R. Polevoi, A. Loarte, R. Dux, T. Eich, E. Fable, D. Coster, S. Maruyama, S.Yu. Medvedev, F. Köchl, and V.E. Zhogolev. Integrated simulations of h-mode operation in ITER including core fuelling, divertor detachment and ELM control. *Nuclear Fusion*, 58(5):056020, mar 2018.